

RSC

Applied Interfaces

Accepted Manuscript

This article can be cited before page numbers have been issued, to do this please use: F. Rohne, D. Vasquez Muñoz, Y. Gordievskaya, C. Braksch, I. Meier, A. Sharma, S. Loebner, A. Nitschke, N. Lomadze, A. Taubert, S. Santer and M. Bekir, *RSC Appl. Interfaces*, 2026, DOI: 10.1039/D5LF00341E.



This is an Accepted Manuscript, which has been through the Royal Society of Chemistry peer review process and has been accepted for publication.

Accepted Manuscripts are published online shortly after acceptance, before technical editing, formatting and proof reading. Using this free service, authors can make their results available to the community, in citable form, before we publish the edited article. We will replace this Accepted Manuscript with the edited and formatted Advance Article as soon as it is available.

You can find more information about Accepted Manuscripts in the [Information for Authors](#).

Please note that technical editing may introduce minor changes to the text and/or graphics, which may alter content. The journal's standard [Terms & Conditions](#) and the [Ethical guidelines](#) still apply. In no event shall the Royal Society of Chemistry be held responsible for any errors or omissions in this Accepted Manuscript or any consequences arising from the use of any information it contains.

1 Phototunable Hopping of Microparticles Enables Surface**2 Selective Continuous Separation via Microfluidics**

3 Fabian Rohne,¹ Daniela Vasquez Muñoz,¹ Yulia Gordievskaya,¹ Cevin Braksch,¹ Isabel
4 Meier,¹ Anjali Sharma,¹ Sarah Loebner,¹ Anne Nitschke,² Nino Lomadze,¹ Andreas Taubert,²
5 Svetlana Santer,¹ Marek Bekir,^{1*}

6 ¹ *Institute of Physics and Astronomy, University of Potsdam, 14476 Potsdam, Germany*

7 ¹ *Institute of Chemistry, University of Potsdam, 14476 Potsdam, Germany*

9 AUTHOR EMAIL ADDRESS: marek.bekir@uni-potsdam.de

11 **RECEIVED DATE**

12 TITLE RUNNING HEAD:

13 **KEYWORDS:** microfluidics; particle separation; surface sensitivity; photosensitive surfactant;
14 light driven diffusioosmosis

15



1

2 **ABSTRACT**

3 High surface area materials are central to next-generation technologies, yet their purification
4 remains limited by lab-scale methods. We present a continuous-flow technique that separates
5 microparticles by surface area and porosity. The method relies on light-responsive surfactants
6 that generate surface-localized photochemical activity under illumination, scaling with particle
7 surface area. Particles with sufficient activity undergo light-induced “hopping” into an
8 overlying channel, enabling deflection across streamlines and obstacles. Non-porous particles
9 remain confined, while porous particles are diverted to secondary outlets. We demonstrate
10 control of hopping efficiency through illumination parameters, establishing a scalable platform
11 for high-throughput, surface-sensitive purification.

12 **Introduction**

13 Next-generation applications increasingly demand advanced functional materials with highly
14 specialized properties. Among the wide array of critical material characteristics, one
15 universally advantageous and frequently required attribute, particularly for dynamic and
16 responsive systems, is a high specific surface area. Materials exhibiting high surface areas offer
17 enhanced interfacial contact with their environment, thereby significantly improving mass and
18 energy exchange processes and enabling a more efficient response to external stimuli.

19 This makes porous microparticles of growing considerable interest, as their high surface-to-
20 volume ratios underpin performance enhancements across a diverse range of technological
21 applications.^[1] These include heterogeneous catalysis,^[2,3,4] next-generation battery
22 systems,^[5,6,7] fabrication of porous 2d macroscopic interfaces with colloidal lithography,^[8]
23 heat-energy storage media,^[9] and adsorption-based technologies such as activated carbon for
24 wastewater treatment,^[10,11,12] among others.^[13,14,15,16] In each of these fields, the porous
25 architecture of the particles directly influences functional efficiency, making morphological
26 control, especially porosity, a central design criterion.

27 However, the scalable fabrication of such porous microparticles remains a significant
28 challenge. Conventional synthesis methods often yield particles with broad distributions in size
29 and structural heterogeneity, particularly in terms of porosity and internal surface area. Such
30 variability can severely compromise performance consistency in end-use applications. For



1 instance, in catalysis or electrochemical energy storage, minor deviations in surface area can
2 lead to disproportionately large drops in activity or capacity.

3 Therefore, beyond size-based classification, it is important to develop strategies for the
4 selective separation and fractionation of particles based on their porosity or, effectively, their
5 accessible surface area. Despite the widespread use of particle sizing techniques at both
6 laboratory^[17,18,19,20,21] and industrial scales,^[22,23,24] methods for surface based (includes porosity
7 based) separation have only recently gained traction, driven largely by advances in surface-
8 chemistry-mediated fractionation approaches.^[25] Recent advances have demonstrated the
9 integration of phoretic or osmotic activity with microfluidic platforms, wherein colloidal
10 particles are suspended in aqueous media containing dissolved salts.^[25] By employing
11 controlled injection protocols to establish localized salt concentration gradients, active colloids
12 can be guided toward specific regions within the microchannel. Under laminar flow conditions,
13 this method facilitates selective migration, segregation, and subsequent collection of particles
14 through spatially separated outlets under continuous operation. Rather than relying on
15 microfluidic-based fractionation techniques, Zheng et al demonstrated that particles can be
16 locally separated and remotely guided to predefined location down to micron scale through
17 spatially controlled light illumination. This approach is enabled by functionalizing the particles
18 with light-responsive dyes, allowing selective manipulation via externally applied illumination
19 patterns.^[26] An alternative approach for particle separation leverages differences in interfacial
20 properties by exploiting surface morphology characteristics such as roughness, porosity, and
21 surface charge. This strategy offers enhanced flexibility, enabling the discrimination of
22 particles with identical sizes but distinct surface chemistries or interfacial compositions.^[27,28]

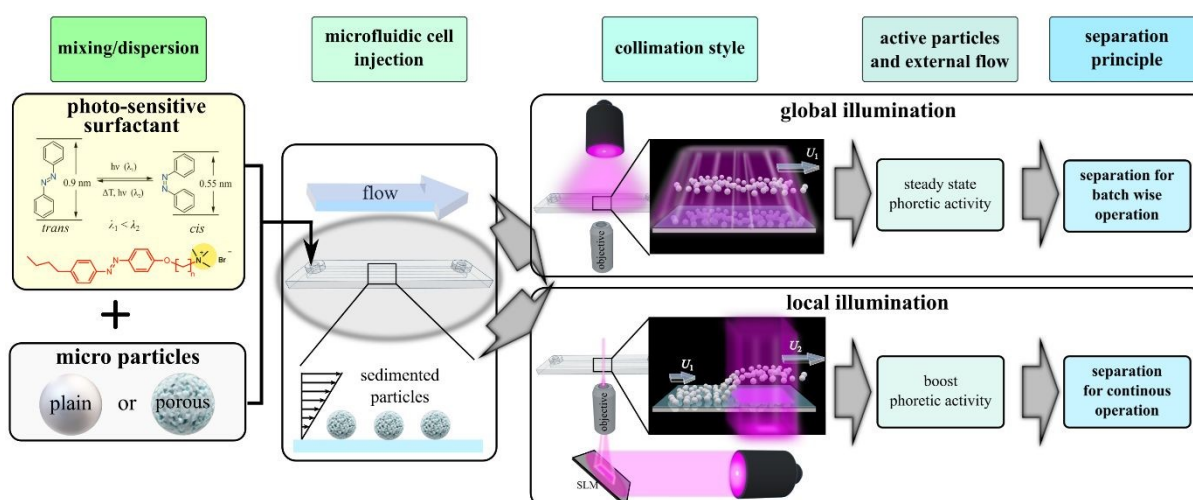
23 Surface-sensitive fractionation can be realized through the integration of microfluidic
24 technology with light-induced phoretic activity of microparticles, as illustrated in **Figure 1**.
25 Initially, microparticles are suspended in a solution containing a photo-responsive surfactant,
26 [(6-[4-(4-Hexylphenylazo)-phenoxy]-butyl-trimethylammoniumbromide, abbreviated AzoC₆,
27 **Figure 1**),^[27] and subsequently introduced into the microfluidic channel. Sedimented
28 microparticles move along with the carrier fluid flow inside the separation cell. Upon
29 illumination, the photo-responsive surfactant renders the particles to be phoretic/osmotic active
30 due to the release of *cis* isomers from particles interface.^[27,28] The bottom wall acts as a
31 reflective boundary for the *cis*-isomers, which cause a hovering of the sedimented particles
32 during light illumination. It has been previously demonstrated that hovering height and



1 translational velocity of the particles depends on the strength of the light induced activity and
2 thus on the interfacial properties of the particles themselves.^[27,28]

3 Two principal illumination strategies may be employed: global^[27,28] and locally^[29] collimated
4 light profiles. In the case of global collimation, as illustrated in **Scheme 1**, the entire separation
5 region is uniformly illuminated. This results in a sustained velocity difference between distinct
6 particle fractions, enabling separation based on retention principles.^[30,31] The method benefits
7 from low-cost instrumentation and straightforward sample preparation; however, its primary
8 limitation lies in throughput.^[28,32] Since the separation process operates in a batchwise manner,
9 it is less suited for high-throughput applications involving large quantities of dispersed
10 particles.

11 To improve the throughput, one needs to transition from a batchwise to a continuous separation
12 mode. This forms the central focus of the present study, in which we propose a framework for
13 continuous, surface-sensitive separation based on locally collimated light illumination, as
14 depicted in **Scheme 1**. In this approach, particles entering the illuminated region experience a
15 transient enhancement in phoretic activity, which can be sufficiently strong to enable them to
16 traverse physical obstacles. Specifically, this activity allows certain particles to be levitated
17 into a secondary, elevated microchannel, from which they are extracted via a separate outlet.
18 Such selective fractionation based on interfacial properties is feasible only for particles
19 exhibiting sufficiently strong light-induced phoretic responses.^[27] For example, only particles
20 with high surface porosity may generate enough propulsion to surmount step heights of
21 approximately 100 μm along otherwise planar interfaces. Such high levitation requires strong
22 phoretic activity, which can be achieved by using the principles of *l*-LDDO only when the
23 applied wavelength is in the UV range.^[33,34,35]



1 **Scheme 1.** Schematic overview of surface sensitive separation principles. (a) Microparticles
2 are dispersed in aqueous solution containing AzoC_6 ($c_{\text{azo}} = 1 \text{ mM}$). (b) After equilibration time
3 ($\sim 1 \text{ day}$) the dispersion is injected into separation cell (microfluidic chamber composed of
4 glass transparent in UV range). Particles sediment at the substrate bottom in the separation cell.
5 (c) Separation principle under global (top) or local light (bottom) illumination. Global
6 illumination causes particles to hover continuously, but only over short distances, leading to
7 velocity differences and separation by elution, similar to gravitational field-flow fractionation.
8 This process is simple but limited to batch operation. In contrast, localized illumination (in
9 particular UV light, $\lambda = 365 \text{ nm}$) induces transient hovering, lifting particles several
10 micrometers into the channel void, where they can enter a second, higher channel position.
11 Under locally collimated light, particles can permanently hop over obstacles, enabling a
12 continuous separation process.

13 We previously demonstrated particle fractionation in batchwise operation using a modified
14 field-flow fractionation (FFF) principle.^[36] This approach was shown to be effective for several
15 distinct particle pair types, including particles with porous versus non-porous interfacial
16 structures,^[27] particles composed of different polymeric materials by tuning the wavelength of
17 the applied illumination,^[28] and particles exhibiting only minor differences in surface
18 functionalization through the use of a chemically active interface.^[32]

19 The approach presented in this work departs from these earlier studies^[27,28,32,36] by translating
20 the separation concept from batchwise to continuous operation. While the same aqueous
21 photosensitive surfactant solution is employed, the separation mechanism is fundamentally
22 changed by replacing global illumination with spatially localized light collimation. This
23 modification enables particle levitation above obstacles and enables continuous selective
24 fractionation of one species. In the following, we first analyze the levitation strength as a
25 function of illumination wavelength, followed by a demonstration of how this effect can be
26 employed as a continuous separation mechanism.

27

28 **Theory: from velocity as a proxy to predict levitation height as a function of the** 29 **wavelength**

30 The levitation dynamics of particles suspended in fluid within a laminar microchannel are
31 strongly governed by the local hydrodynamic environment. Owing to their comparatively large
32 mass and micron-scale dimensions, yet still being much smaller than the characteristic
33 geometric length scale of the channel (height = 0.54 mm), the particles undergo gravitational
34 sedimentation. Consequently, they remain confined to a narrow near-wall region, either in
35 direct contact with the bottom surface or levitated only a few micrometers above it. In this
36 regime, the local flow field can be approximated by a linear shear profile, consistent with low-



1 Reynolds-number hydrodynamics under Stokes flow conditions. When a particle is levitated at
 2 a height h_{ac} above the lower wall (see for illustration **Figure S1**), it is situated in a region of
 3 laminar flow with a spatially varying velocity gradient. In this regime, conservation of mass
 4 and momentum leads to the development of a net drift velocity U , which scales with the local
 5 shear rate S . This shear rate is evaluated at a vertical position equal to the sum of the particle
 6 radius and levitation height, $h_{ac} = a + h_{lev}$, where the flow profile remains approximately linear.
 7 Consequently, the particle's translational motion is governed by its hydrodynamic interaction
 8 with the spatially varying flow field at that elevation. Under the assumption that particles are
 9 positioned at the mid-width of a rectangular microchannel (**Scheme 1**) Brenner *et al.* derived
 10 an asymptotic expression,^[37,38] where the hovering tendency is connected with translational
 11 velocity as:^[27,28,37,38,39]

$$U = S \cdot h_{ac} \cdot \left(1 - \frac{5}{16} \cdot \left(\frac{a}{h_{ac}}\right)^3\right) \quad \text{Eq. 1}$$

12 where S is the applied shear rate, a the particle radius and h_{ac} the hovering height of the
 13 particle. If the hovering is much larger than the particle radius $h_{ac} \gg a$ the asymptotic
 14 expression $\frac{5}{16} \cdot \left(\frac{a}{h_{ac}}\right)^3$ is very small and can be omitted in first approximation. This assumption
 15 holds true for strongly hovered particles discussed later in the results and discussion section
 16 under local light collimation. Then **Eq. 1** simplify into:

$$U \sim S \cdot h_{ac} = S \cdot (a + h_{lev}), \quad \text{Eq. 2}$$

17 where per definition (see **Figure S1**) h_{ac} is the sum of particle radius plus the minimum
 18 separation distance between the bottom particle surface and the channel substrate, thus
 19 $h_{ac} = a + h_{lev}$. From **Eq. 2** we calculate the value of levitation height:

$$h_{lev} \sim \frac{U}{S} - a. \quad \text{Eq. 3}$$

20

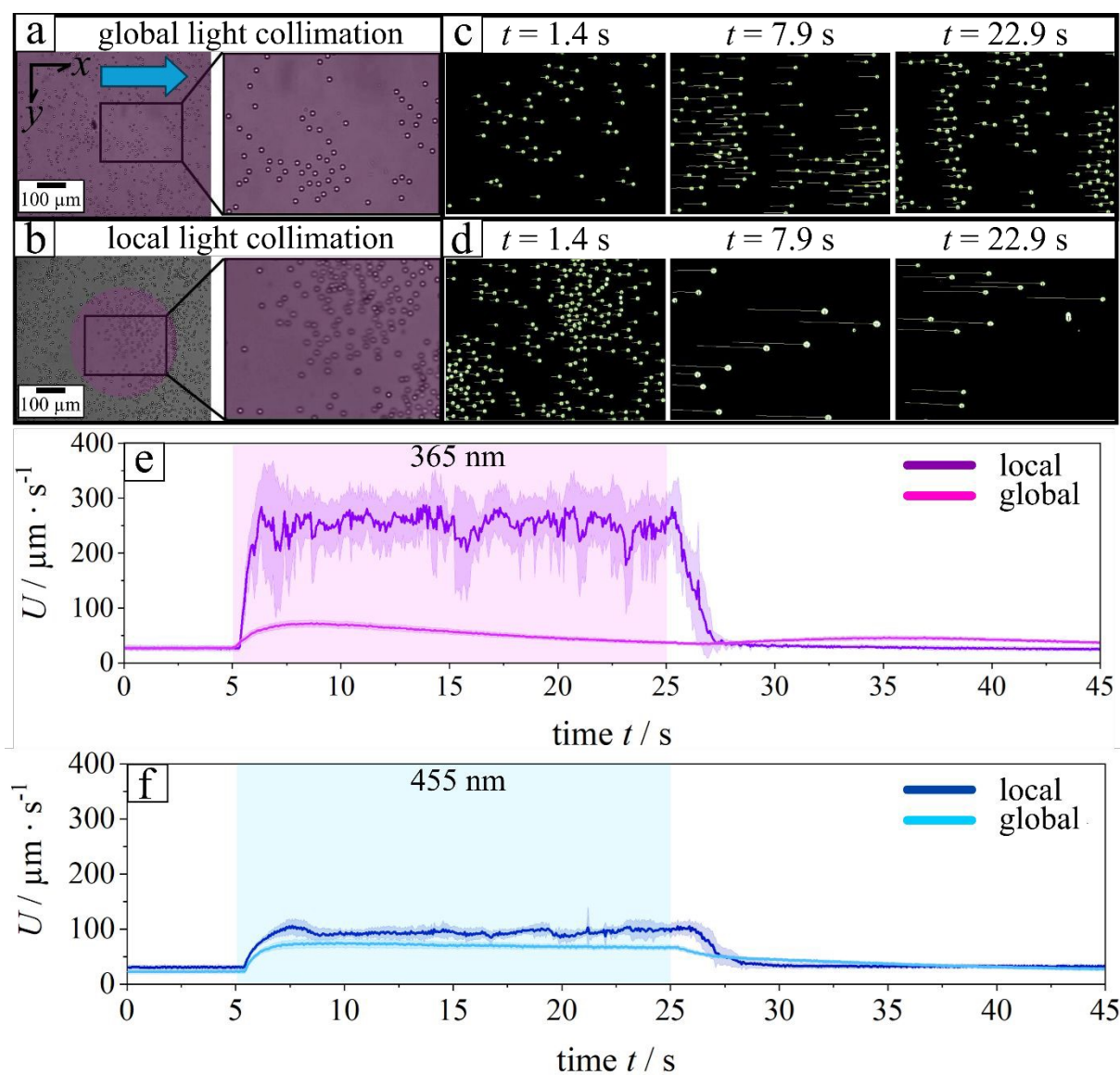
21 Results and Discussion

22 Systematic investigation of velocity boost as a function of the wavelength

23 Before introducing the concept of continuous separation, we first address the rationale for
 24 employing UV light illumination. This choice is motivated by a systematic investigation of
 25 particle hovering behavior as a function of illumination wavelength. In all experiments, two



1 illumination strategies were implemented: local and global collimation. The corresponding
 2 illuminated regions are shown for UV light in **Video S1** and as snapshot series in **Figures 1a-**
 3 **d**. Particle motion was quantified by tracking individual trajectories across the illumination
 4 region. For each frame, the mean particle velocity was calculated from all crossing trajectories,
 5 and the temporal evolution of the average velocity (bold line) together with the standard
 6 deviation (shaded region) is reported for local (**Figures 1b,d**) and global collimation (**Figures**
 7 **1a,c**). All experiments were conducted in a rectangular microfluidic channel (height $h = 0.54$
 8 mm, width $w = 3.8$ mm, length $L = 17$ mm) at a constant volumetric flow rate of $150 \mu\text{L}/\text{min}$,
 9 corresponding to a shear rate of 14.98 s^{-1} as determined from **Eq. 13 (Materials and Methods**
 10 **Section)**.



11

12 **Figure 1.** (a,b) Snapshots illustrating the two illumination strategies: (a) globally and (b)
 13 locally collimated UV light ($\lambda = 365 \text{ nm}$) at identical applied power ($P = 11.45 \text{ mW}$). Data are



1 taken from **Video S1**. (b,d) Processed images with particle trajectories over a 1 s recording
2 window, shown before illumination (1.7 s), during illumination (7.9 s), and after switching off
3 the light (22.9 s). (c) Corresponds to global illumination, (d) to local illumination. (e) Time-
4 resolved average velocity obtained from trajectory analysis for **Video S1** (365 nm) and (f) for
5 **Video S2** (455 nm).
6

7 Under local light collimation and particularly for UV light data exhibit a constant strong boost
8 of entering microparticles and thus the average velocity maintains for the whole-time frame of
9 illumination, while at global light particles experience a transient boost with subsequent decay
10 to the initial velocity at no illumination. It is important to note that collimation from the bottom
11 substrate minimizes the optical path length through the microfluidic channel. This improves
12 the boosting tendency of chemical activity of the microparticles and strongly impact the
13 levitation height.

14 The average steady-state velocity, plotted in **Figure 3c,d** for the final 5 s of illumination ($t =$
15 $20\text{--}25$ s), reveals that light-induced motion varies not only in velocity profile as a function of
16 wavelength but also in absolute magnitude. Velocities under local illumination (see **Figure 3c**)
17 are consistently higher compared to global collimation (see **Figure 3d**). Although the applied
18 power was kept constant in all experiments ($P = 11.5$ mW), local collimation through the
19 objective confines the light to a rectangular spot of only a few micrometers ($200 \times 300 \mu\text{m}$),
20 additionally loses power output leaving the objective to 0.8 mW, thereby substantially
21 increasing the local intensity. This enhanced intensity amplifies the phoretic/osmotic activity,
22 which scales with light intensity. As a result, particles exhibit stronger activity, attain larger
23 hovering heights (h_a), and reach higher velocities in agreement with **Eq. 1**. In the following,
24 we discuss in more detail the differences in motion patterns between the two collimation
25 strategies.

27 **Global light illumination**

28 For global light illumination, a detailed explanation has already been provided in Ref. [28] and
29 the corresponding Supporting Information. In brief, the phoretic/osmotic activity arises from
30 the formation of a *cis*-isomer gradient and is therefore governed by the photoisomerization
31 kinetics at the microparticle interface. A highly simplified description that considers only the
32 *cis*-isomer conversion rate at the interface cannot capture all details (for a comprehensive
33 discussion, see Ref. [28]), but it conveys the essential trend: the particle velocity varies
34 systematically with illumination wavelength:



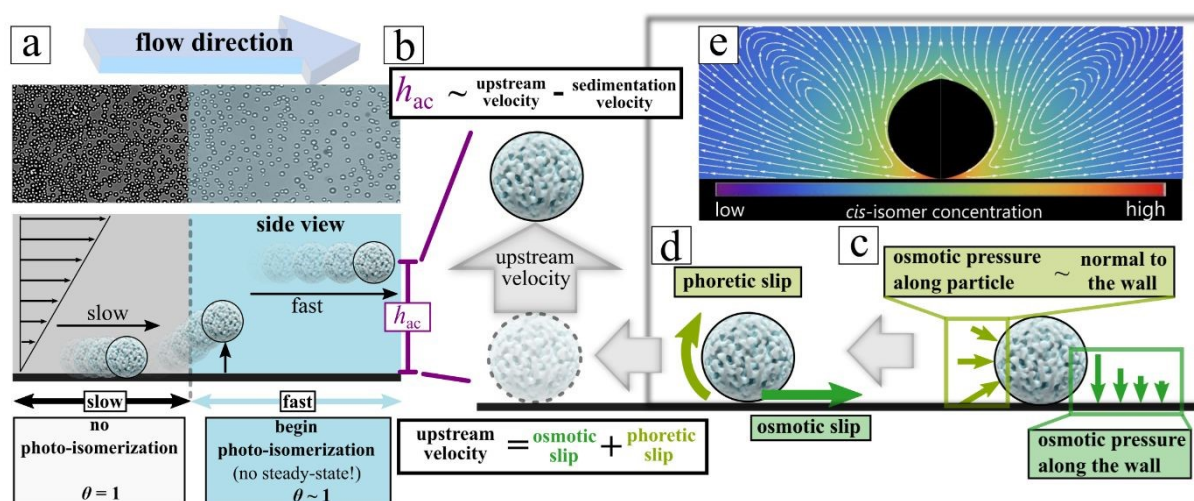
$$\text{constant flux} \sim \frac{dc_p}{dt} = k_{TC,I}(\lambda) \cdot I \cdot A_{\text{eff}} \cdot \theta_T \quad \text{Eq. 4}$$

1 with I as applied light intensity, $k_{TC,I}$ the photoisomerization rate constant at given wavelength,
 2 A_{eff} the effective surface area of the particles and θ_T as the *trans* isomer surface coverage. Two
 3 key parameters are of significant importance, the value of $k_{TC,I}$ and θ_T . Now, the decrease of
 4 applied wavelength yields in a decrease in the value of $k_{TC,I}$ and increase of the value of the
 5 *trans*-isomer surface coverage, θ_T . The latter results from an increase of the *trans* isomer
 6 fraction with increasing wavelength.^[28] This cause the *cis* isomer conversion rate (\sim *cis* isomer
 7 flux), basically the product of both, to peak at a maximum for 405/415 nm of radiation
 8 wavelength and so follows the translation velocity due to hovering, too (**Figure 3d**).^[28]

9 Local light collimation

10 For local light collimation the general assumption of phoretic activity connected by the relation
 11 **Eq. 4** holds true as well but with only one difference that the surface coverage of *trans* isomers,
 12 θ_T is always 1 instead in global light collimation to be fraction between 0 and 1. Then **Eq. 4**
 13 simplifies into:

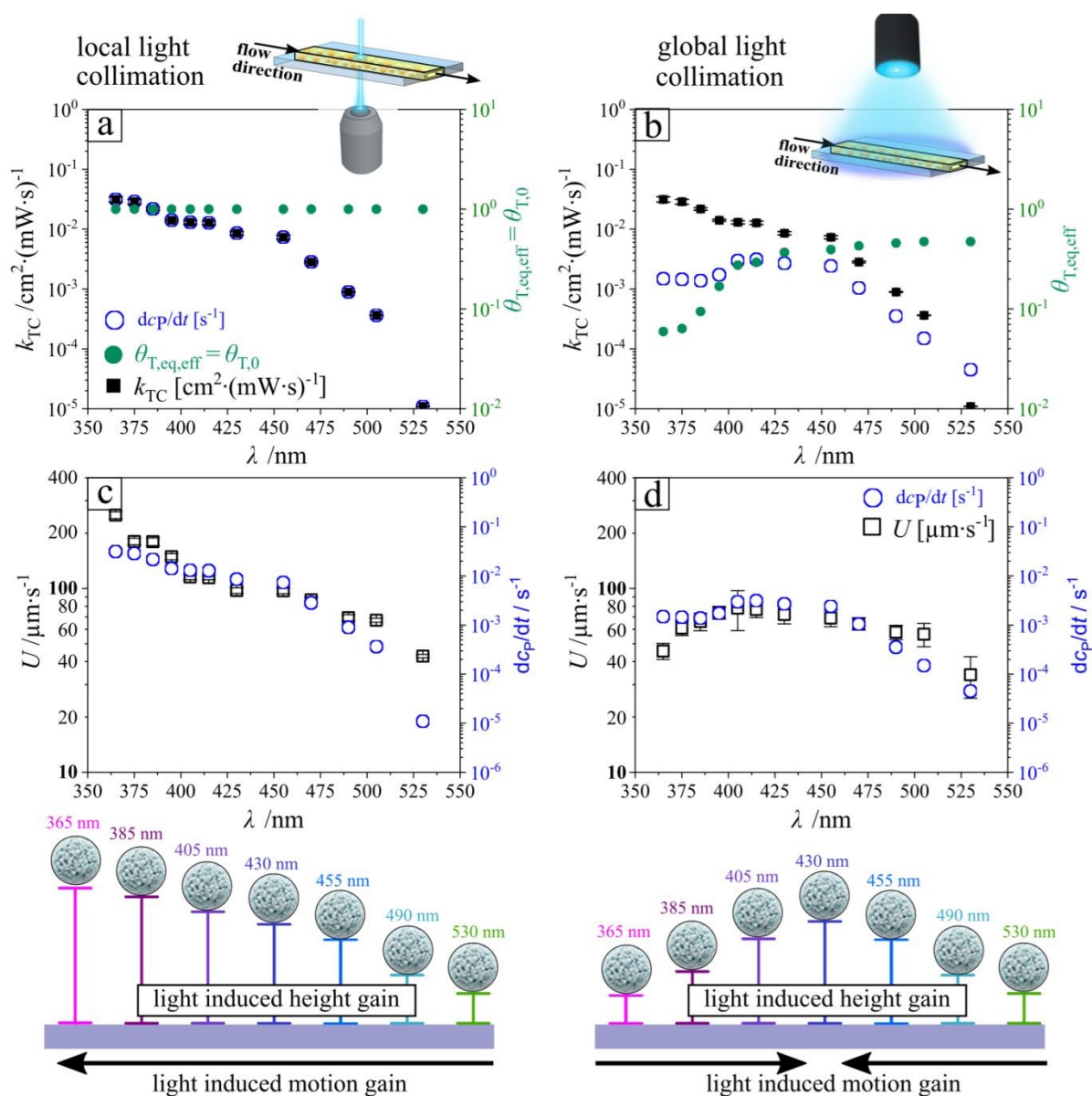
$$\text{constant flux} \sim \frac{dc_p}{dt} = k_{TC,I}(\lambda) \cdot I \cdot A_{\text{eff}} \quad \text{Eq. 5}$$



14 **Figure 2.** (a) Optical micrograph (top) and schematic side view (bottom) of porous
 15 microparticles entering the illuminated area, where surface coverage of *trans*-isomers is
 16 maximal ($\theta = 1$). Dynamic exchange has not yet reached steady state, so the interface remains
 17 fully covered. Blue arrow: flow direction. (b) Phoretic activity lifts the particles to an
 18 equilibrium height h_{ac} , defined by the balance of light-induced upstream and sedimentation
 19 velocities. Osmotic (dark green) and phoretic (olive green) contributions are indicated. (c)
 20 Local *cis*-isomer concentration gradients form around the particles (purple = low c_{cis} , red =
 21 high c_{cis} ; white arrows: fluid flow). (d) Vertical and horizontal osmotic pressure gradients (olive,
 22 dark green) decay into the bulk and control the light-induced upstream velocity.
 23



1
2 Upon entering the illuminated region (**Video S3**), particles experience photoisomerization in
3 both bulk solution and at their interface, leading to complete *trans*-isomer coverage. Over the
4 crossing time (~ 4 s), this coverage remains effectively unchanged, as the induced velocities
5 prevent significant depletion. We therefore assume $\theta_T = 1$ for all particles within the illuminated
6 area. Under this condition, the velocity exhibits a linear dependence on the photoisomerization
7 rate constant $k_{TC,I} = k_{TC}$ and the effective particle area A_{eff} , consistent with experimental
8 observations (**Figure 3**).



9
10 **Figure 3.** Key photochemical parameters under local (left, a,c) and global (right, b,d)
11 illumination. (a,b) Steady-state isomer flux, d_{cp}/dt , *trans*-isomer coverage θ_T , and *trans*-to-*cis*
12 rate constant k_{TC} as a function of wavelength, indicating local photoactivity and effective *l*-
13 LDDO strength. (c,d) Corresponding particle velocities under the same spectral conditions,

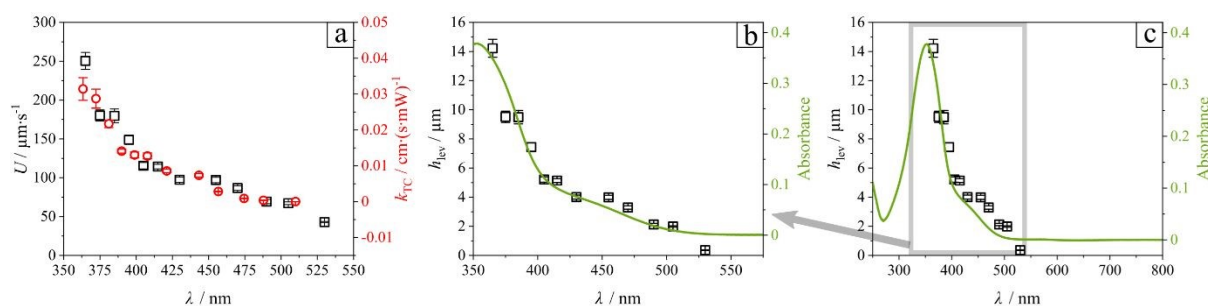


1 differing only in illumination geometry. Data in (b,d) are reproduced from Ref. [28] to highlight
 2 the impact of illumination collimation on particle dynamics. Note, that local light collimation
 3 from the bottom of the substrate minimizes the optical pathway and drastically improves the
 4 boosting in levitation.

5 Data exhibit that the velocity follows the pattern of the *trans* isomer absorption spectrum. We
 6 explain this relation by the fact that the value of the photoisomerization rate constant is the
 7 product of the quantum yield ϕ , the extinction coefficient ε and the applied intensity of
 8 illumination I :^[40]

$$k_{\text{photoisomerization}} = \phi \cdot \varepsilon \cdot I. \quad \text{Eq. 6}$$

9 And since the intensity already has been extracted here out^[33] and kept fixed, the magnitude of
 10 the velocity and hovering height is proportional to $\varepsilon_T(\lambda)$ for each wavelength, due to
 11 $\sim U(\lambda) \sim h_{\text{ac}}(\lambda) \sim k_{\text{TC}}(\lambda) \sim \varepsilon_T(\lambda)$. This means that under local illumination one can approximate the
 12 light induced levitation strength (**Figure 4b,c**) and translational velocity boost of particles
 13 (**Figure S3b,c**) from the absorbance spectrum of the photo switch. Apparently, the *trans* isomer
 14 has a peak maximum at 351 nm and so the velocity boost is the strongest in UV range with
 15 increasing value towards blue shift. This means the strongest levitation of microparticles can
 16 be expected under illumination in UV range (**Figure 4bc,c**).



17
 18 **Figure 4.** (a) Particle velocity under spectrally resolved illumination (dark hollow rectangles)
 19 overlaid with the *trans*-to-*cis* isomerization rate constant k_{TC} (red hollow circles), showing the
 20 spectral dependence of drift motion. (b, c) Measured hovering height (dark hollow rectangles)
 21 is compared with the UV-vis absorbance of the *trans*-isomer ($c = 0.1$ mM), highlighting the
 22 correlation between spectral absorption and light-induced motion. A corresponding velocity
 23 plot is provided in **Figure S3 (Supporting Information)**.

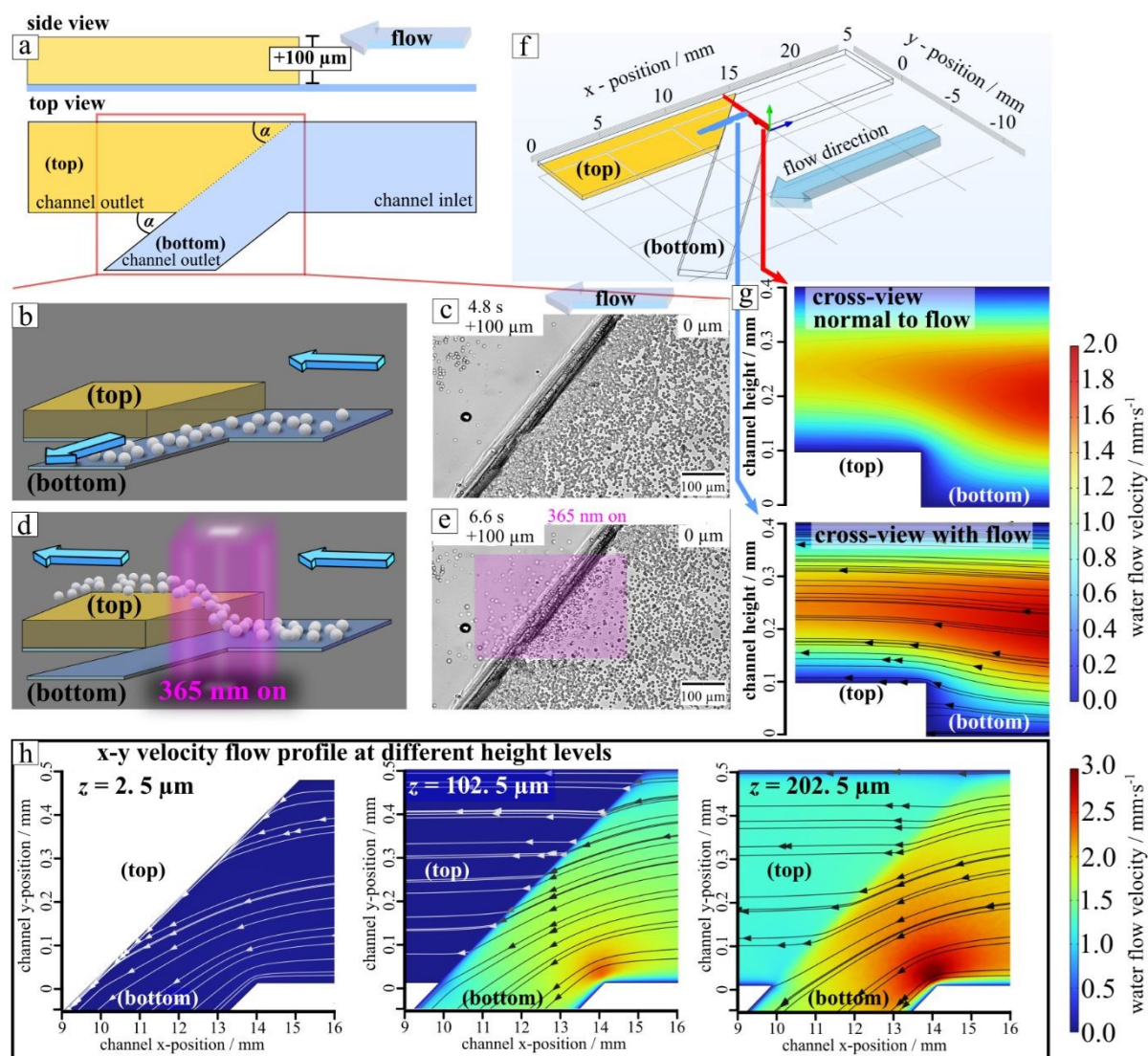
24

25 *Hovering of particles over obstacles for continuous separation*

26 Strong levitation allows microparticles to cross obstacles taller than their diameter, provided
 27 they exhibit sufficient phoretic activity. We demonstrate this by hovering 5 μm porous particles
 28 over a 100 μm wall (two tape layers; **Video S4, Figures 5c,e**). The wall is angled $\sim 40^\circ$ to
 29 deflect passive momentum and reduce accumulation. UV illumination enables on-demand



- 1 “hop on/hop off” motion over the wall, allowing remote guidance of particles along different
 2 streamlines.



- 3
 4 **Figure 5.** Conceptual strategy for continuous microparticle separation based on surface
 5 properties using light-induced levitation in a laminar flow channel. (a) Schematic of the
 6 microfluidic separation device: cross-sectional side view (top) and top view (bottom). (b,c)
 7 Under dark conditions, sedimented particles introduced at the channel inlet remain near the
 8 bottom and are guided by laminar flow into Outlet (bottom). (b) Schematic particle trajectories;
 9 (c) optical micrograph from **Video S4** at $t = 4.6$ s (light off) confirming sedimentation-guided
 10 flow. (d,e) Upon localized UV illumination ($\lambda = 365$ nm), porous particles levitate and are
 11 redirected to Outlet (top). (d) Micrograph from **Video S4** at $t = 6.6$ s (light on) showing particle
 12 levitation; the vertical displacement (~ 100 μm) is achieved with two layers of transparent tape.
 13 (f) COMSOL simulation geometry of the laminar flow field; blue arrow indicates flow
 14 direction. Red and blue rectangles mark cross-sectional planes orthogonal and parallel to flow,
 15 respectively. (g) Flow field simulations at 150 $\mu\text{L}/\text{min}$ for transverse (y - z , top) and longitudinal
 16 (x - z , bottom) planes; color indicates local velocity (mm/s). (h) Simulated top-view (x - y plane)
 17 flow velocities at three vertical positions: 2.5 μm (particle radius), 102.5 μm (channel height +
 18 particle radius), and 202.5 μm (above channel). These results illustrate how vertical particle
 19 position influences experienced flow, guiding separation behavior.



1 Apparently, we observe that the levitation of the particle can be lower than the height of the
 2 obstacle as data in **Figure 5e** and **Video S4** clearly demonstrate a wall lift migration, while
 3 calculated levitation height h_{lev} is much lower. We estimated the needed minimum elevation
 4 height of particles by calculating the value of h_{lev} using Eq. 3 in absence of any obstacle, where
 5 the applied illumination intensity has been precisely varied displayed in **Figure S5a**. Then we
 6 compared the value of h_{lev} with the hopping potential over the obstacle by performing same
 7 measurements with same variation in intensity displayed in **Figure S5b**. Data exhibits that
 8 already $5 \mu\text{m}$ of levitation, approximately one diameter, is enough to successfully hop particles
 9 over the obstacle. Thus, besides the light induced levitation, hydrodynamic effects appear to
 10 play a critical role in the system, particularly in regions proximal to obstacles, where particle
 11 lift forces are significantly amplified. In general, when particles are in close proximity to
 12 channel walls or the bottom substrate, they experience a transverse pressure gradient. This
 13 gradient induces a hydrodynamic lift force directed away from the lower boundary (substrate)
 14 toward the center of the channel. This near-wall lift force F_{Nw} given by:^[41,42,43]

$$F_{Nw} = \frac{6 \cdot C \cdot \eta \cdot a^3}{h_{lev}} \cdot S \quad \text{Eq. 7}$$

15 where, C is the empirical, dimensionless coefficient; η the dynamic viscosity of the carrier
 16 fluid; S the local shear rate of the fluid near the channel bottom substrate; a the radius of the
 17 suspended particle; and h_{lev} the minimum separation distance between the particle surface and
 18 the channel wall. As the particle moves away from the substrate, the hydrodynamic lift force
 19 increases until it counterbalances the gravitational force at a specific equilibrium position. In
 20 regimes where inertial contributions to the lift force are negligible (i.e., low Reynolds number
 21 or Stokes flow conditions), the net force is given by:

$$F_{net} = F_{Nw} - F_G = \frac{6 \cdot C \cdot \eta \cdot a^3}{h_{lev}} \cdot S - \frac{4}{3} \cdot a^3 \cdot \Delta\rho \cdot G, \quad \text{Eq. 8}$$

22 where F_G is the gravitational force acting on the particle, with a density difference $\Delta\rho$ relative
 23 to the carrier fluid, G the gravitational acceleration, typically taken as $9.81 \text{ m}\cdot\text{s}^{-2}$. At
 24 equilibrium position the force $F_{net} = 0$ and Eq. 8 can be rewritten into:^[44]

$$h_{lev} = \frac{9}{2} \cdot \frac{C \cdot \eta}{\Delta\rho \cdot G} \cdot S. \quad \text{Eq. 9}$$

25 In other words, particles according to density migrate under shear already to a certain elevation
 26 zone depending on the fluid velocity (\sim shear rate S) but are independent of the particle size.
 27 This is irrespective of the light induced levitation. Now when particles come close to the



1 obstacle the local laminar flow field may yield to additional perturbation and influences shear-
2 induced rotation of the particle, i.e. increases near-wall lift force F_{Nw} . Note, neither **Eq. 1-Eq.**
3 **3** nor **Eq. 9** are valid for flow fields close to the proximity to obstacles. This means a stronger
4 lift force might appear, where light induced hovering is additionally manipulated.

5 Thus, to further support the demonstration of the separation potential of hopping particles
6 traversing diagonal obstacles, we perform numerical simulations of the fluid flow field using
7 the COMSOL Multiphysics software. The simulation domain is illustrated in **Figure 5f**, and
8 representative cross-sectional velocity field profiles are presented in **Figure 5g** both in the
9 plane normal to the flow (top) and along the flow direction (bottom). As shown in **Figure 5g**,
10 the computed flow streamlines indicate that fluid can only traverse around the obstacle at
11 specific vertical (z) positions within the microchannel. And if the light induced hovering
12 reaches the critical vertical position the remaining distance can be overcome from the carrier
13 fluid.

14 Notably, at an elevation corresponding to the particle radius ($z = 2.5 \mu\text{m}$), streamlines are
15 directed from the vicinity of the wall toward outlet channel (bottom) (**Figure 5h**, left). This
16 result aligns with experimental observations from **Video S4**, where microparticles are passively
17 advected along the wall when the illumination is off. At higher vertical positions specifically
18 at the top of the obstacle ($z = 102.5 \mu\text{m}$, **Figure 6h**, middle) and significantly above it ($z = 202.5$
19 μm , **Figure 5h**, right) the flow streamlines are directed toward the upper outlet channel (top),
20 with some extend in lateral deflection toward outlet (bottom). These flow characteristics
21 correspond well with experimental trajectories of particles that are transiently elevated under
22 UV illumination, demonstrating the influence of vertical position on particle routing via the
23 local flow field.

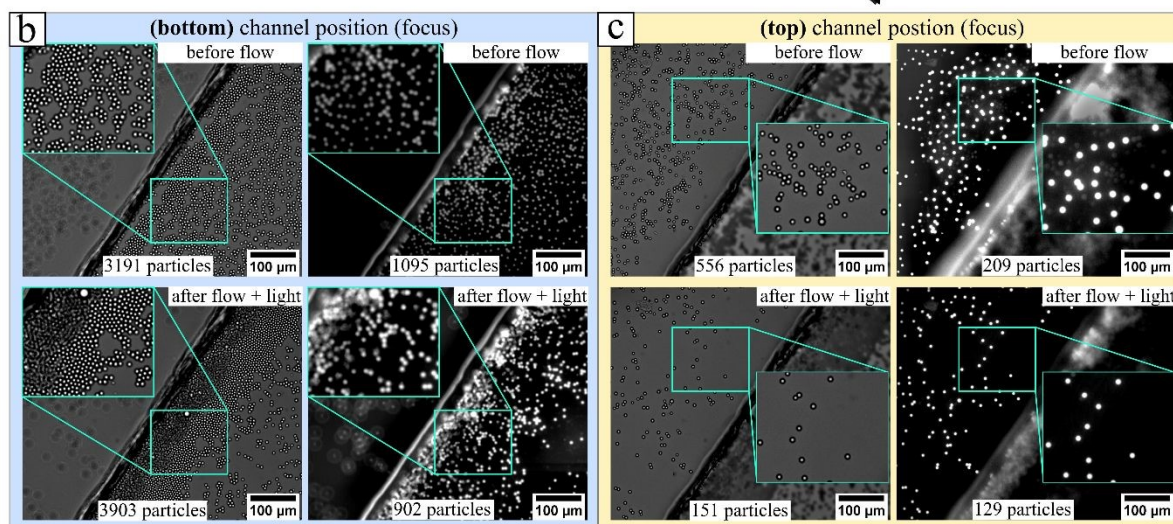
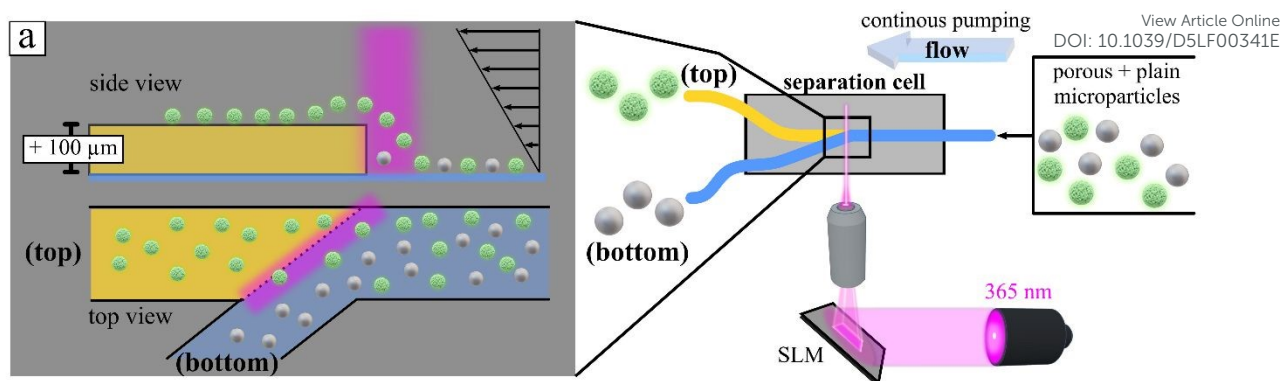
24 The hopping principle can be used to selectively fractionate particles based on interfacial
25 properties. Levitation over high obstacles requires strong phoretic activity, which scales with
26 the effective surface area A_{eff} and determines the *trans-to-cis* isomer flux. Under UV
27 illumination (365 nm), porous particles with large A_{eff} levitate higher, whereas plain particles
28 with small A_{eff} show negligible lift. A binary mixture of porous and plain particles thus
29 separates, with porous particles elevated into the higher channel while plain particles remain
30 below (**Figure 6**, **Video S5**). Fluorescein dye in the solution enhances emission from porous
31 particles, providing a visual confirmation of selective levitation during simultaneous UV
32 illumination and emission microscopy.^[45,46] The pronounced elevation observed for the porous



1 particles can be attributed to their substantially increased specific surface area compared to that
2 of the plain particle interface. An influence arising solely from differences in intrinsic surface
3 charge between the two particle types can be excluded. As shown in **Figure S4**, both silica
4 microparticle systems exhibit comparable negative zeta potentials in aqueous medium,
5 consistent with the presence of deprotonated surface hydroxyl groups. Upon addition of a
6 cationic surfactant (1 mM), both particle types display a positive zeta potential, which can be
7 ascribed to the adsorption of the surfactant and the formation of a multilayer at the particle
8 interface at the given concentration.^[47] Under UV irradiation, the zeta potential remains
9 positive but decreases in magnitude. This reduction is attributed to photoisomerization-induced
10 desorption processes: the predominance of *cis* isomers leads to partial desorption, resulting in
11 a reduced surface coverage by the remaining *trans* isomers in accordance with the *trans/cis*
12 population ratio.^[47] These observations confirm that the distinct elevation behavior of porous
13 particles is not governed by differences in net surface charge, but rather by their enhanced
14 interfacial area and the associated amplification of interfacial interactions.

15 Furthermore, we note that particle inertia is negligible under the investigated flow conditions.
16 Consequently, the light-induced hopping behavior is interpreted to be governed primarily by
17 advection along the streamlines rather than inertial effects. Based on the theoretical
18 considerations presented in the literature,^[36] we calculated a Stokes number ($St \approx 3.32 \cdot 10^{-4}$)
19 much smaller than 1 for the system as detailed in Supporting Information Section S8. The
20 obtained result confirms that inertial contributions are minimal and do not significantly
21 influence the particle dynamics.





separation efficiency for plain $\text{SiO}_2 = 0.77$

separation efficiency for (porous) $\text{PSiO}_2 = 0.85$

Figure 6. Experimental demonstration of selective separation of identically sized microparticles based on surface morphology. Microparticles ($5 \mu\text{m}$) with porous (PSiO_2) or plain (SiO_2) surfaces were separated using light-guided levitation in a microfluidic device. (a) Schematic of the separation principle: upon entering the localized UV-illuminated region (“light gate”), porous particles levitate transiently due to enhanced *l*-LDDO, allowing transport via laminar flow into the upper outlet (top). Plain SiO_2 particles lack sufficient levitation and remain near the lower surface, exiting via Outlet I. Statistical or structural variation means not all porous particles cross, but the approach enriches porous particles in Outlet II. (b,c) Optical micrographs from **Video S5** before and after separation, captured at the bottom (Outlet I) and top (Outlet II) planes. Each panel shows bright-field and fluorescence (FITC channel) images: porous particles exhibit stronger emission than plain particles, enabling optical differentiation and confirming enrichment in the upper outlet. Details on separation efficiency are provided in Supporting Information Section S5.

Furthermore, to quantify the separation efficiency over an operation time of 30 s separation we calculated the number of particles in bright field and emission recording before and after separation. Bright field recording reveals the total number of all particles, porous and plain particles together, so $N_{\text{PSiO}_2} + N_{\text{SiO}_2}$, while emission recording reveals only the porous particles, N_{PSiO_2} . Thus, one has all important information to calculate the separation efficiency, SE, with respect to porous microparticles equals the fraction of porous particles:



$$SE = \frac{N_{\text{PSiO}_2}}{N_{\text{PSiO}_2} + N_{\text{SiO}_2}} = \frac{N_{\text{emission}}}{N_{\text{brightfield}}},$$

View Article Online
DOI: 10.1039/D5LF00341E

Eq. 10

1 similar as used in our previous publications.^[27,28] We calculated the separation efficiency
 2 before and after the illumination for both channel positions on top of and on the bottom wall
 3 labeled in **Figure 6** as bottom or top focus. To demonstrate the change in SE during separation
 4 upon UV light illumination we quickly injected the mixture of plain and porous microparticles
 5 ($\text{SiO}_2/\text{PSiO}_2 = 2/1$) to achieve a homogenous distribution of the particles over the entire
 6 microfluidic chamber, thus we have initially equal population below and above the wall.
 7 Therefore, in the beginning we measured on top (top) a binary fraction of plain and porous
 8 particles (**Figure 6c**) in a ratio of $SE_{\text{PSiO}_2} = 0.37 = 209/556$, in reasonable agreement with
 9 adjusted particle population. After running the demonstration separation upon light activation
 10 displayed in **Video S5** we observe the porous (bright emitting) microparticles to hop over the
 11 wall. Then after the separation data exhibit in **Figure 6c** a dominating fraction of porous
 12 particles with a measured $SE_{\text{PSiO}_2} = 0.85 = 129/151$. The efficient enrichment of porous
 13 particles in the upper outlet (top) confirms the effectiveness of light-induced levitation and
 14 microfluidic separation, as most plain particles remain confined to the lower channel. This
 15 performance highlights the selectivity of the method, since only particles with strong phoretic
 16 activity linked to their porous surface can overcome the wall barrier under UV illumination
 17 and reach Outlet II. The separation efficiency (SE) is not perfect, with approximately 15 % of
 18 plain particles still observed in the upper outlet. Detailed inspection reveals doublets of porous
 19 and plain particles (inset, **Figure 6c**), where a porous particle can transiently carry a plain
 20 particle into the higher channel. Although relatively rare, such particle-particle interactions
 21 illustrate the influence of dynamic aggregation on the composition and purity of the separated
 22 porous fraction.

23 Analyzing now the bottom channel (bottom) initially we have a binary mixture of plain and
 24 porous particles with a ratio of $0.34 = 1095/3191$, in good agreement with value for the initial
 25 top channel to be 0.37. After separation we observe a strong accumulation of plain particles,
 26 yet porous particles are still present, and it yields according to Eq. 10 a SE_{PSiO_2} for porous to
 27 be $0.23 = 902/3903$. Given the fact that we expect at the bottom channel (bottom) an enriched
 28 population of plain particles accordingly the value of $SE_{\text{SiO}_2} = 1 - SE_{\text{PSiO}_2}$ and yields a value of
 29 0.77 demonstrating an accumulation of the plain particle in the same order as for the porous in
 30 the upper channel. Quantification in the bottom channel should be approached with caution, as
 31 cumulative stacking of multiple particles leads to a significant increase in concentration,



1 making precise particle counting impossible. Although the mixture is clearly not purified, the
2 visible multilayer formation of plain particles indicates that these particles comprise the
3 dominant fraction.

4 From **Video S5 (Figure 6)**, we demonstrated selective fractionation of porous particles.
5 Continuous flow allows new particles to be hovered into the upper channel (top) while others
6 are deflected into the lower channel (bottom) by the 40° wall angle. This enables continuous,
7 surface-sensitive separation of particles with strong osmotic/phoretic activity, i.e., those with
8 large surface areas. In this example, porous and plain silica particles of equal size were
9 separated. We emphasize that a direct quantitative relationship between surface area and
10 chemical activity cannot be established due to several additional factors, including surfactant
11 diffusion within pores, surface functionalization, and electrostatic interactions. These factors
12 may either limit or enhance the dynamic exchange of *trans-cis* isomers under illumination,
13 thereby affecting the effective activity (e.g., the measured $U(\lambda)$). This conclusion is drawn from
14 a comparison between surface areas measured via nitrogen sorption and surface areas inferred
15 from chemical activity measurements.^[35] Nitrogen sorption measurements indicate an
16 approximately fifth-fold larger pore volume for porous particles compared to non-porous
17 particles displayed in **Figure S21** (data taken from reference),^[48] whereas an approximately
18 33-fold stronger chemical activity is reported for the same system in the absence of external
19 flow.^[35] This might be attributed that the effective average pore diameter of the porous particles
20 is measured 12 nm, in comparison to non-porous particles to be 2.5 nm (see **Figure S21b**),
21 which is in the dimension of the surfactant molecule size to be approximately 2 nm.^[49] Thus
22 the strength in chemical activity and the separation potential shown in this work critically
23 depends on the pore size.^[48] A detailed discussion is provided in the Supporting Information
24 (Section S6).”

25 Unlike traditional batch-based methods, such as chromatographic or flow-field fractionation,
26 ^[27,30,31,39] this approach allows continuous operation, enhancing throughput and efficiency. To
27 substantiate this claim, we estimate the mass throughput of fractionated porous particles by
28 quantifying the number of particles crossing the obstacle within the detection area shown in
29 Video S5. Specifically, number of crossing particles were counted within a region of
30 $360 \cdot 410 \mu\text{m}^2$ over an observation period of 30 s under continuous illumination.

31 The calculation in Section S9 (Supporting Information) and data presented in Figure S20
32 indicate that, assuming a homogeneous particle concentration across the channel width w ,
33 approximately 1585 particles per second are deflected into the upper channel via hydrodynamic
34 levitation. Considering a particle diameter of $5 \mu\text{m}$ and a material density of 1.8 g cm^{-3} , this



1 corresponds to a processed sample mass of approximately 0.672 mg h^{-1} during one hour of
2 continuous operation. Although the resulting throughput remains within the milligram range,
3 thus being primarily suited for laboratory-scale applications, it exceeds the throughput reported
4 for comparable batch-wise fractionation strategies in the literature^[27,30,31,39] by roughly two
5 orders of magnitude.

6 For comparison, batch-based fractionation typically requires at least 20 min per cycle to
7 achieve complete binary separation under quiescent conditions. In addition to the separation
8 time itself, several preparatory and post-processing steps are required: particle collection after
9 separation, reinjection of a fresh suspension into the separation chamber, careful reconnection
10 of pumping tubes to avoid air bubble formation within tubing and the separation cell, and the
11 re-establishment of fully sedimented initial conditions. These auxiliary procedures generally
12 require an additional preparation time of approximately 10 min. Consequently, a single
13 operational cycle, including separation and preparation, takes about 30 min, allowing for only
14 two cycles per hour of operation. Under these conditions, the achievable sample throughput
15 amounts to approximately 0.004 mg h^{-1} . This comparison clearly demonstrates that the
16 continuous fractionation scheme substantially enhances processing efficiency, increasing the
17 achievable sample throughput by a factor of approximately 160 relative to conventional batch-
18 based methodologies.^[27,30,31,39]

19 The principle of separation relies on temporarily hovering particles from a lower to a higher
20 wall position via microfluidics and illumination of a photoswitchable surfactant at an
21 appropriate wavelength, easily optimized using UV-vis spectroscopy. For continuous
22 separation, it is essential that the injected particles fully sediment onto the bottom substrate
23 before encountering the obstacle. From the injection point to the separation wall, particles are
24 transported along streamlines according to the local flow velocity at their respective vertical
25 positions within the channel.

26 To provide a simplified estimate of the required sedimentation time and the corresponding
27 horizontal travel distance (i.e., the minimum required injection channel length), we assume that
28 the microparticles are introduced at the top of the rectangular microfluidic channel (i.e., at h).
29 Furthermore, we assume that the sedimentation velocity is not significantly influenced by the
30 perpendicular laminar flow, since it introduces no turbulence in the system. Accordingly, the
31 description of the sedimentation velocity by a low Reynolds number is rectified. Under this
32 assumption, the buoyancy-corrected gravitational force is balanced by the viscous drag force
33 according to Stokes' law, allowing estimation of the terminal sedimentation velocity.



1 Additionally, the particle will follow the streamlines of the laminar flow inside the microfluidic
2 channel during sedimentation. The motion along the streamlines of the laminar flow is
3 perpendicular to the sedimentation motion. Hence, we can calculate the sedimentation time
4 ($t_{\text{sed}} = 107.5$ s, see Section S7 in the Supporting Information) independently of motion along
5 the laminar flow, and then calculate the distance traveled along the flow, which is 44 mm.
6 Accordingly, the distance between the injection point and the separation wall should be at least
7 44 mm or longer (See detailed calculations in the Section S7, Supporting Information).

8 Furthermore, precise adjustment of the local illumination position relative to the wall is
9 essential. For accurate positioning of the illumination spot, it is crucial that the particles reach
10 their maximum levitation height at the moment they cross the wall or obstacle. This
11 requirement arises because the levitation process is not instantaneous: particles typically
12 require approximately 3–4 seconds after illumination to reach their fully developed hovering
13 state. Accordingly, the time required for levitation must match the longitudinal travel time of
14 the particles toward the obstacle, such that maximum levitation aligns with the crossing of the
15 obstacle. In our previous study, we mapped the particle velocity field (x–y position) under
16 localized UV illumination on a planar substrate and observed that the maximum levitation
17 height was attained after the particles had traveled a defined distance following UV
18 excitation.^[36] Consequently, the illumination spot should be positioned at a corresponding
19 upstream distance on the order of 160 μm before the particles encounter the wall. An increase
20 in flow rate extends the longitudinal distance traveled within the same levitation time under
21 identical illumination conditions. Therefore, with increasing flow rate, the distance between
22 the local light spot and the obstacle must be increased proportionally to ensure that maximum
23 levitation is achieved at the point of crossing.

24 Additionally, we recommend employing the highest possible light intensity in order to generate
25 the strongest transient levitation enhancement. For strong light-induced chemical activity, as
26 required for the temporal hopping of particles over obstacles, the appropriate choice of
27 surfactant concentration is crucial. The total surfactant concentration should be well above the
28 CMC of the *trans* isomer ($\text{CMC}_{\text{trans}} = 0.5$ mM). This ensures that even under illumination, a
29 sufficient fraction of *trans* isomers remains in solution, allowing a rapid dynamic exchange
30 between adsorbing *trans* molecules (with adsorption rate proportional to concentration) and
31 desorbing *cis* molecules.^[35] This dynamic exchange sustains a pronounced *cis*-isomer gradient
32 in the vicinity of the particles and thereby maintains strong light-induced chemical activity.
33 Only above a critical *trans*-isomer concentration does the interface remain fully covered with



1 *trans* molecules. At total surfactant concentrations of 2 mM or higher, the interface remains
2 saturated even under UV illumination,^[47,50] whereas at lower concentrations significant net
3 desorption at water–glass interfaces has been reported.^[50] At the same time, concentrations
4 exceeding 4 mM should be avoided, as this corresponds to the CMC of the *cis* isomer
5 (CMC_{cis} = 4.0 mM). In this regime, the *cis* isomer itself becomes surface-active, which reduces
6 the *cis* concentration gradient and consequently weakens the chemical activity. Therefore, in
7 the experiments presented in this work, the surfactant concentration was set to 1 mM,
8 representing a regime well above CMC_{trans} yet below CMC_{cis}, thereby ensuring robust and
9 reproducible light-induced levitation

10 Future improvements include tuning wall height to increase selectivity for less active particles
11 and adjusting wall angles to minimize accumulation of non-hovered particles. Overall, the
12 results demonstrate the feasibility of continuous, surface-sensitive particle separation in
13 microfluidic devices and highlight the potential for further optimization for high-purity, high-
14 throughput applications.

15 To upscale and generalize the continuous separation principle based on selective light-induced
16 hopping of one particle fraction across others, two boundary conditions are critical: (i) a
17 sufficiently high activity contrast between particle fractions, and (ii) at least one fraction
18 exhibiting intrinsically strong chemical activity. In the following, we qualitatively discuss key
19 engineering parameters governing transferability and scale-up of the separation concept, with
20 particular emphasis on surface/material properties, particle concentration, and the choice of
21 photosensitive surfactant.

22 Surface and Material Properties

23 Light-induced levitation of microparticles has been demonstrated for a broad range of
24 interfacial systems, including porous interfaces,^[27,28] chemically functionalized surfaces
25 (hydrophobic and hydrophilic moieties),^[27,32] and polymer-modified microparticles.^[31] For
26 many of these systems, the *l*-LDDO strength is moderate, resulting in equilibrium levitation
27 heights on the order of 1–2 μm above the bottom substrate. For overcoming macroscopic
28 obstacles (e.g., >100 μm), however, a substantially higher levitation force is required. Since
29 the applied photosurfactant carries a cationic headgroup,^[51] preferential adsorption is expected
30 at anionic interfaces,^[47] particularly those with high specific surface area. Consequently,
31 negatively charged and porous materials (e.g., silica-based particles^[27,28] and activated carbon)
32 are anticipated to exhibit enhanced interfacial surfactant accumulation and thus stronger *l*-



1 LDDO activity. Similarly, microgels and highly hydrated polymer networks, especially those
2 incorporating anionic functional groups can generate pronounced chemical gradients under
3 illumination.^[52] From a separation engineering perspective, these material classes provide a
4 larger activity contrast window and are therefore particularly suitable for selective fractionation
5 based on light-triggered hopping over obstacles.

6 **Particle Concentration Effects**

7 The hopping mechanism is comparatively robust over several orders of magnitude in particle
8 concentration.^[36] However, experimental observations indicate that levitation height decreases
9 with increasing particle number density.^[36] This behavior can be attributed to collective effects
10 such as local depletion of product gradients. As a result, the effective activity contrast between
11 fractions reduces with increasing concentration, rendering selective separation progressively
12 more challenging. The extent of this limitation depends on the natural light induced activity
13 strength of the respective particle fractions. For scale-up considerations, concentration-
14 dependent transport phenomena therefore represent a key parameter.

15 **Photosensitive Surfactant Selection**

16 The choice of photosensitive surfactant constitutes a central control parameter in the separation
17 process. In the present study, an azobenzene-based cationic surfactant was employed, for which
18 photoisomerization kinetics in bulk^[33] and at interfaces,^[35,50] as well as adsorption/desorption
19 dynamics at solid–liquid interfaces (with^[50] and without illumination^[47]), have been
20 extensively characterized in the literature. Reported kinetic data indicate that the relative rates
21 of adsorption/desorption and photoisomerization enable a sustained dynamic exchange
22 between *trans*- and *cis*-isomers under continuous illumination. This dynamic steady state
23 generates sufficiently strong and spatially confined chemical gradients at solid-liquid-
24 interfaces to induce active levitation of microparticles in aqueous media. Importantly, the
25 propulsion strength and equilibrium position can be precisely modulated via illumination
26 wavelength^[28] and intensity,^[36] providing a high degree of external process control.

27 Variations in hydrophobic chain length and headgroup architecture of the surfactant molecule
28 significantly affect interfacial packing density,^[53] adsorption equilibria, and desorption kinetics
29 of both isomers, and therefore directly modulate the magnitude of the light-induced chemical
30 activity. While LDDO has been reported for surfactants with different alkyl chain lengths, the
31 strongest effects to date have been observed for the compound presented in **Figure 1**. Current
32 literature suggests that cationic headgroups with minimal steric demand promote higher



1 interfacial accumulation compared to bulkier analogues,^[53] thereby enhancing gradient
2 formation.

3 Nevertheless, the selection of an optimal photosensitive surfactant is inherently application-
4 specific and multidimensional, involving trade-offs between molecular volume change upon
5 isomerization, photostability, quantum yield, adsorption strength, and dynamic exchange
6 potential.^[53] Among available photoresponsive systems,^[54,55,56,57,58] azobenzene derivatives
7 remain particularly attractive due to their pronounced conformational change during
8 isomerization and low photodegradation, albeit at moderate quantum yield.^[59] The latter can
9 be compensated by applying high photon flux (i.e., increased illumination intensity), enabling
10 high conversion rates and sustained gradient formation.^[27,28] For a comprehensive discussion
11 on material-specific classification of light-induced chemical activity and surfactant selection
12 strategies, the reader is referred to the corresponding perspective article published
13 elsewhere.^[53]

14
15

16 **Conclusion**

17 We demonstrated that with the combination of a photoactive surfactant and microfluidics one
18 can separate equally sized microparticles by their differences in their interface, where the
19 principle of separation could run continuously.

20 The principle works by hovering sedimented particles over obstacles/walls much bigger than
21 the size of the particles. To that end particles are induced osmotically/phoretically active, which
22 produces, leads to selective levitation of only strongly active particles. Then, simultaneously,
23 an external fluid flow carries the particles in an upper channel position. Now particles with
24 difference in surface properties likewise porous versus plain particle are hovering differently
25 high and by so, only the porous (~ strong active) can be guided into the higher channel. The
26 plain particles remain effectively non-hovered and are deflected from the wall, where the flow
27 guides them into the lower channel. Such strong levitation requires locally collimated light
28 through the microscope objective, which not only focuses on the applied light intensity but also
29 needs a special wavelength of illumination. Both parameters must increase the initial burst
30 (~initial photoisomerization kinetics) of adsorbed trans-isomers by that porous particles are
31 temporary so strong active to pass by a wall lift height of 100 μm . For azobenzene containing
32 surfactants such strong activities could be achieved with UV light (365 nm).



1 To predict the wavelength needed for high levitation (~strong activity) of the particles, this can
2 be estimated from the extinction coefficient of the photo switch, a strait forward value quickly
3 to be obtained from UV-vis spectroscopy. The physical principles result from the
4 photoisomerization rate constant, which is proportional to the extinction coefficient.

5

6 **Materials**

7 **Microfluidic chambers and microparticles:** Microfluidic experiments were conducted using
8 commercially available flow chambers (μ -Slide^{VI}, Ibidi GmbH), featuring a glass-bottom
9 coverslip suitable for high-resolution optical microscopy. Each chamber has a void volume of
10 40 μ L.

11 Two types of silica-based colloidal particles were employed in the study: Commercial porous
12 silica microparticles with mean diameters of (3 ± 1) μ m and (5 ± 1) μ m, otherwise unmodified,
13 were obtained from micromod GmbH (sicastar® 43-00-503). These particles possess internal
14 porosity. Non-porous (plain) silica colloids with narrowly distributed diameters of (4 ± 0.1)
15 μ m and (5 ± 0.1) μ m otherwise unmodified, were sourced from microparticles GmbH (SiO₂-
16 F-SC260-2).

17

18 **Azobenzene containing surfactant**

19 The azobenzene-containing surfactant, **C₄-Azo-OC₆TMAB** (azobenzene-functionalized
20 trimethylammonium bromide), was synthesized in accordance with previously reported
21 methodologies. Structurally (Figure 1), the molecule consists of a cationic trimethylammonium
22 bromide headgroup connected to an azobenzene core via a hexamethylene spacer. The
23 azobenzene unit is further functionalized with a terminal butyl chain, enhancing its amphiphilic
24 character.

25 A stock solution of the surfactant was prepared at a concentration of 10 mM in ultrapure water
26 (Milli-Q, resistivity > 18 M Ω ·cm) and subsequently diluted to 1 mM for experimental
27 applications involving microparticle dispersions.

28 The photophysical behavior of the surfactant was characterized via UV-visible absorption
29 spectroscopy (**Figure 1c**). In its thermodynamically stable *trans*-configuration, the molecule
30 exhibits a prominent π - π^* transition centered at 351 nm. Upon photoisomerization to the *cis*-
31 isomer, the absorption profile changes markedly, showing a blue-shifted π - π^* transition at 313
32 nm and the emergence of an n- π^* transition at 437 nm. The *cis*-isomer is metastable and
33 undergoes thermal relaxation back to the *trans*-form with a half-life of approximately 48 hours



1 under ambient dark conditions or under continuous red-light irradiation ($\lambda = 625 \text{ nm}$) at 23
2 °C.^[33]

4 ***Sample Preparation***

5 Aqueous colloidal dispersions are mixed with a stock solution of photosensitive surfactants to
6 reach a final surfactant concentration of 1 mM. The mixtures are equilibrated for a minimum
7 of 24 hours prior to any measurements to ensure homogeneous distribution and equilibration
8 of the surfactant within the dispersion. For measurements, the surfactant–colloid mixture is
9 introduced into the microfluidic chamber, where gravitational sedimentation leads to the
10 accumulation of particles on the bottom glass surface. The chamber is connected to a syringe
11 pump (PhD Ultra, Harvard Apparatus), enabling controlled fluid manipulation. The entire
12 fluidic system including the chamber, syringe, and connecting tubing is prefilled with the same
13 aqueous solution containing 1 mM of the photosensitive surfactant to maintain chemical
14 consistency throughout the setup. All samples are handled and stored under red light or in the
15 dark to prevent unintended photo-isomerization of the azobenzene-containing surfactant.
16 Measurements are carried out at ambient conditions, with the temperature maintained at
17 $T = 23 \pm 1 \text{ °C}$.

18 ***Sample preparation with fluorescein dye***: Fluorescein was used as the fluorescent probe for
19 all emission imaging experiments. Prior to mixing with particle mixture of porous (PSiO₂) and
20 plain (SiO₂) particles ($D = 5 \text{ }\mu\text{m}$, $c_{\text{particles, total}} = 0.3 \text{ mg/mL}$, ratio SiO₂/PSiO₂ = 2/1), the
21 surfactant solution ($c = 1 \text{ mM}$) is mixed with fluorescein ($c = 15 \text{ }\mu\text{M}$). Similar as above, the
22 entire fluidic system including the chamber, syringe, and connecting tubing contain the
23 surfactant-dye solution. Details of measurement conditions are shown in **Supporting**
24 **Information (Section S4)**.

26 **Preparation of Modified Glass Substrate for Microfluidic Integration**

27 A standard borosilicate microscope glass slide (commercially available) was modified to create
28 a patterned surface suitable for microfluidic chamber. Two parallel layers of transparent
29 pressure-sensitive adhesive tape (Tesa GmbH) were applied to the substrate surface. These tape
30 layers were aligned and trimmed such that the resulting boundary edges formed an angle of
31 45° relative to the anticipated fluid flow direction within the final microfluidic chamber.
32 Selective regions of the adhesive tape, corresponding to the future microchannel area, were
33 carefully scraped using a precision utility blade under light pressure to avoid damaging the
34 underlying glass. This defined the channel bottom substrate of the microfluidic channel.



1 Following the tape removal, residual adhesive in the exposed regions was immediately cleaned
2 using a minimal volume of high-purity methanol. The cleaning was performed with care to
3 minimize solvent interaction with the remaining adhered tape sections, preserving their
4 integrity. The substrate was then left to dry under ambient conditions until complete methanol
5 evaporation was confirmed.

6 Subsequently, the cleaned and patterned glass substrate was aligned and bonded to a
7 commercial microfluidic channel (sticky-Slide VI^{0.4}, Ibidi GmbH), which incorporates a pre-
8 defined chamber geometry. The microfluidic channel dimensions are approximately: length
9 $L = 17$ mm, width $w = 3.8$ mm, and height $h = 0.54$ mm corresponding to a void volume of
10 approximately $30 \mu\text{L}$.

12 ***Zeta potential measurements***

13 Zeta potential is calculated from the electrophoretic mobility measured using commercial zetasizer
14 (Nano-ZS, Malvern Instruments, Ltd., Malvern, UK). Microparticles ($c_{\text{mass}} = 0.1$ mg/ml) are dispersed
15 in MilliQ or aqueous solution containing the azobenzene surfactant solution ($c = 1$ mM). Prior to
16 measurements dispersion are sonicated and immediately injected into the measurement cell, an directly
17 measured. Data containing UV illumination is exposed for 12 min under irradiation with UV light
18 (365 nm, $I = 10$ mW/cm²), followed by sonication for 10 s.

20 ***Nitrogen sorption analysis***

21 The porous and non-porous commercial stock colloidal suspension was purified by two successive
22 washes with Millipore-grade water to eliminate residual contaminants. The cleaned suspensions were
23 subsequently freeze-dried overnight under high vacuum (<1 mbar) using a Schlenk line. The resulting
24 dry powders and approximately 100 mg were used for N₂ sorption.

25 **Nitrogen sorption measurements:**

26 Prior to analysis, the dried samples were accurately weighed, transferred into analysis cells, and
27 degassed under vacuum at 300 °C for 3 h using a BELPREP VAC III preparation system (Microtrac).
28 Nitrogen adsorption–desorption isotherms were recorded with a BELSORP MAX surface area and
29 porosity analyzer (Microtrac). Depending on the porosity of the samples, measurement times ranged
30 from 18 h (porous particles) to 43 h (non-porous particles). Adsorption data are presented as the
31 adsorbed nitrogen volume plotted against the corresponding relative pressure.

34 ***COMSOL Simulations***



1 COMSOL Multiphysics 6.3 (COMSOL Inc., Burlington, MA) was used to simulate fluid flow
2 The model was implemented in 3D using a finer, physics-controlled mesh consisting of
3 4974542 domain elements, 286916 boundary elements, and 6669 edge elements. (**Figure S4**).
4 Flow within the system was modeled under steady-state laminar conditions with a fixed
5 volumetric flow rate of 150 $\mu\text{L}/\text{min}$, since Reynolds number under study is low, $\text{Re} \sim 100$. A no-
6 slip boundary condition was applied to all walls.

7 *Image acquisition and light source*

8 An inverted optical microscope (Olympus IX73) equipped with dual-wavelength illumination
9 capabilities was employed for sample observation and photoactivation. The illumination
10 system enabled both global and localized exposure of the sample to two distinct wavelengths:
11 625 nm (red) and a secondary wavelength denoted as X nm.

12 The 625 nm wavelength served as image acquisition tool, as it does not induce photo-
13 isomerization of the photosensitive surfactant. In contrast, the secondary wavelength (X nm)
14 was selected based on its ability to induce photo-isomerization. The LED illumination system
15 was configured to enable both global and localized collimation. For global illumination, the
16 light was collimated through the ocular pathway, resulting in uniform exposure across the
17 entire sample area. For localized illumination, the light beam was first shaped using a spatial
18 light modulator (SLM), enabling precise spatial control of the illumination pattern. The
19 modulated beam was then directed through the objective lens to selectively illuminate defined
20 regions of the sample at the focal plane.

21 This dual-mode collimation approach allowed flexible photoactivation strategies, facilitating
22 both homogeneous and spatially resolved control of light-responsive surfactants. A detailed
23 schematic of the optical setup and beam collimation pathways is provided in **Figure S10**
24 (Supporting Information, Microscope Setup).

25 After transmission through the sample, all wavelengths below 625 nm were effectively blocked
26 using a 580 nm long-pass optical filter (Thorlabs GmbH), thereby ensuring that only the red
27 light (625 nm) reached the detection system. This optical filtering enabled selective imaging
28 under non-photoactivating conditions, minimizing interference from photoresponsive
29 wavelengths during video acquisition. All LED light sources used in the study were obtained
30 from Thorlabs GmbH, with the following center wavelengths and model numbers: 365 nm
31 (M365LP1), 375 nm (M375L4), 385 nm (M385L3), 395 nm (M395L5), 405 nm (M405L4-
32 C1), 415 nm (M415L4), 430 nm (M430L5), 455 nm (M455L4), 490 nm (M490L4), 505 nm
33



1 (M505L4-C1), 530 nm (M530L4), and 625 nm (M625L4). Video recordings were performed
 2 using a Hamamatsu ORCA-Flash camera at a frame rate of 30 frames per second, capturing
 3 dynamics exclusively under red-light illumination.

4 **Fluorescence imaging**

5 Fluorescence imaging was performed using the inverted microscope equipped with standard
 6 FITC filter sets (excitation: 488 nm; emission: 500–550 nm). Fluoresceine fluorescence was
 7 excited using the white light source Xe-Hg light source, where low band pass filter was used
 8 for spectral excitation range 350–490 nm. This allows a simultaneous illumination of UV light
 9 for photoisomerization of the surfactant to hop up the particles and the excitation of the dye.
 10 Emission was collected using a 505–530 nm high bandpass filter. Images were acquired using
 11 a objective with 20 x magnification/ 0.4 NA and are processed using the software package
 12 Fiji/Image. Imaging parameters such as light source power, gain, and exposure time (0.5 s)
 13 were held constant between experimental conditions to enable bright emissions of porous and
 14 a weak emission of non-porous particles.

15 **Kinetic investigations**

16 Photoisomerization rate constants were analyzed and published on our previous
 17 publication.[28] Briefly: UV–Vis kinetics were recorded using a Cary 5000 UV–Vis
 18 spectrophotometer (Agilent Technologies, USA) by using its kinetics module. A quartz cuvette
 19 (Helma Analytics) with 1 cm spacing was filled with 1.8 mL of the aqueous sample and sealed
 20 to maintain constant concentration. The entire sample volume was uniformly irradiated with
 21 an LED at wavelength λ , and absorbance at 376 nm was monitored, normalized to its initial
 22 value, and fitted to the following exponential isomerization model:
 23
 24

$$\frac{Abs_{376}(t)}{Abs_{376,0}} = \frac{c(t)}{c_0} = \frac{k_{CT} + k_{TC} \cdot \exp(-[k_{TC} + k_{CT}] \cdot I \cdot t)}{k_{TC} + k_{CT}} = \frac{k_{CT} + k_{TC} \cdot \exp\left(-\frac{t}{\tau}\right)}{k_{TC} + k_{CT}} \quad \text{Eq. 11}$$

25 here, t is the time, I is the light intensity, k_{TC} and k_{CT} are the *trans*→*cis* and *cis*→*trans*
 26 photo-isomerization rate constants, respectively, and $\tau = 1/[(k_{TC} + k_{CT}) \cdot I]$

27 This allows calculation of k_{TC} given by:

$$k_{TC} = \frac{1}{\tau \cdot I} - \frac{c_{eq}}{c_0} \cdot \frac{1}{\tau \cdot I} \quad \text{Eq. 12}$$



1 Light intensity at the sample location was measured prior to each experiment using a Thorlabs
 2 S170C power meter and set to 1 mW/cm² for UV–Vis studies (and 11.5 mW for microscopy).
 3 Detailed derivations, interpretation and model description are published elsewhere.^[28]

5 ***Volumetric Flow Rate to Shear Rate***

6 The shear rate S for a rectangular channel geometry with channel dimensions: length $l = 17$
 7 mm, height $h = 0.54 \mu\text{m}$ and width $w = 3.8 \text{ mm}$ (experimental conditions in this work) is
 8 calculated by the expression: ^[60]

$$S = \frac{Q}{2 \cdot h^2 \cdot w} \left[\frac{1}{12} - \frac{16h}{\pi^5 w} \right]^{-1}, \quad \text{Eq. 13}$$

9 where Q is the adjusted volumetric flow rate equal to 150 $\mu\text{L}/\text{min}$ always, which correspond to
 10 a shear rate $S = 14.98 \text{ s}^{-1}$.

12 **Video Tracking**

13 Motion videos were acquired using an inverted Olympus microscope (IX73) equipped with a
 14 Hamamatsu ORCA-Flash 4.0 scientific CMOS camera or Olympus MFD 2 – IX53, 73.

15 Depending on the configuration, frame rates were set to 30 fps (ORCA-Flash 4.0) or 15 fps
 16 (MFD2-controlled IX53/IX73).

17 Image acquisition was conducted under red illumination ($I = 0.5 \text{ mW}/\text{cm}^2$) to minimize
 18 photochemical disturbances. For illumination, a collimated LED at wavelength λ was directed
 19 either from above over the condenser (global illumination) or from below over the objective
 20 (illumination) depending on experimental requirements. Prior to each recording session, the
 21 aqueous surfactant solution ($c = 1 \text{ mM}$) with pre-dispersed microparticles was irradiated at λ
 22 for 1 minute at a power of 11.5 mW to ensure attainment of photo-stationary state and
 23 equilibrium isomer population. Motion recording was performed by previously sedimented all
 24 microparticles onto the bottom glass interface of the rectangular microfluidic channel with 17
 25 mm channel length, 3.8 mm channel depth and 0.54 mm channel height ($\mu\text{-slide}^{\text{VI}}$ with a glass
 26 bottom cover slip (Ibidi GmbH).

27 A typical 45-second motion-recording sequence captures microparticle trajectories along flow
 28 streamlines with the following precisely defined illumination protocol:

- 29 1. Initial Phase (0–5 s)
 30 A 5-second period without irradiation, allowing observation of baseline particle
 31 motion under passive flow conditions.



2. Irradiation Phase (5–25 s)

A 20-second interval of illumination at wavelength X ($I = 11.5 \text{ mW/cm}^2$), activating photoresponsivity behavior while continuously recording particle dynamics.

3. Post-illumination Phase (25–45 s)

A final 25-second interval without irradiation, capturing relaxation or persistent effects in the absence of light.

This structured timing ensures a controlled analysis of both the immediate and lasting photo driven responses of the microparticles within the flow system. Each measurement was performed under applied constant pressure driven flow using a syringe pump (Ph.D. ultra, Havard apparatus) with a flow rate of $150 \mu\text{L}/\text{min}$.

Motion analysis of particles

Image analysis was performed by converting grayscale video frames into binary images via a thresholding procedure, wherein background pixels were assigned to a value of zero (black) and particle pixels a value of one (white). Particle tracking was achieved by determining the displacement of the center of mass of each identified particle between two frames. At each time step, the momentum particle velocity was computed for each particle and averaged over all particles present within the field of view. These mean velocities were recorded as a function of time, with the corresponding standard deviation representing the frame-wise variability among particles. For analyses involving summarized time-average quantities, only data collected after the system achieved a steady-state velocity were included. Steady-state was operationally defined as the period commencing 15 seconds after the onset of continuous illumination. We used a python software with several software packages: Bokeh, Numpy, OpenCV-python, Matplotlib, Openpyxl, Pandas, SciPy.^[27,28,32]

Statistical Analysis: Statistical analysis is done similar to our previous publication^[27,28,32] with same set of software Python software package. We calculated the time resolved average velocity U from the sample size n (number of particles) of individual velocity U_i for each frame-to-frame and we averaged using the arithmetic mean to obtain:

$$\bar{U} = \frac{1}{n}(\sum_{i=1}^n U_i) \quad \text{Eq. 14}$$

and the corresponding standard deviation, denoted by σ , computed as the square root of the unbiased sample variance using a denominator of $n-1$, where n is the sample size:



$$\sigma = \sqrt{\frac{1}{n-1} \sum_{n=i} (U_i - \bar{U})^2} .$$

View Article Online
DOI: 10.1039/D5LF00341E
Eq. 15

1 All data is treated without evaluation of outliers.

2

3 **ACKNOWLEDGMENTS.** M.B. acknowledges financial support by the National German
4 Science Foundation (DFG) through the grant BE 7745/1-1. A.T. and A.N. acknowledge
5 funding from the University of Potsdam (grant 5317000).

6 **Author contributions**

7 M.B. designed and supervised the project and wrote the manuscript. F.R., D.V.M performed
8 experiments, analysis, and wrote manuscript together with S.S. C. B., I. M., S. L. and A.S. performed
9 experiments and analysis. N.L. synthesized the photosensitive surfactant. Y. G. performed COMSOL
10 simulations. All the authors were involved in the preparation of the manuscript. All the authors have
11 read and approved the final manuscript.

12

13 **Competing financial interests**

14 The authors declare no competing financial interests.

15

16



1

2 **References**

- [1] X. Yang, F. Yu, H. Shang, Z. Li, S. Wang, Y. Xing and X. Gui, *Powder Technology*, 2025, **453**, 120594.
- [2] Y. Deng, Y. Cai, Z. Sun, J. Lia, C. Liu, J. Weng, W. Li, C. Liu, Y. Wang and D. Zhao, *J. Am. Chem. Soc.*, 2010, **132**, 24, 8466.
- [3] M. A. M. Gijs, F. Lacharme and U. Lehmann, *Chem. Rev.*, 2010, **110**, 1518.
- [4] Y. Ding, Y. Yan, H. Wang, X. Wang, T. Hu, S. Tao and G. Li, *ACS Appl. Mat. Interfaces.*, 2018, **10**, 48.
- [5] H. Kim, B. Han and J. C. Prof., *Angewandte Inter. Ed.*, 2008, **47**, 10151–10154
- [6] H. Liu, X. Liu, W. Li, X. Guo, Y. Wang, G. Wang and D. Zhao, *Advanced Energy Materials*, 2017, **7**, 1700283
- [7] A. Bielefeld, D. A. Weber and J. Janek, *The Journal of Physical Chemistry C*, 2018, **123**, 1626–1634.
- [8] Y. Wang, M. Zhang, Y. Lai and L. Chi, *Nano Today*, 2018, **22**, 36–61.
- [9] Y. Kim, X. Dong, S. Chae, G. Asghar, S. Choi, B. Jun Kim, J.-Y. Choi and H. K. Yu, *Adv. Mater.*, 2022, **35**, 2204775.
- [10] R. Ahmed, I. Block, F. Otte, C. Günter, A. Duarte-Rodrigues, P. Hesemann, A. Banerji and A. Taubert, *Chemistry*, 2023, **5**, 1124–1137.
- [11] S. Wong, N. Ngadi, I. M. Inuwa and O. Hassan, *Journal of Cleaner Production*, 2018, **175**, 361–375.
- [12] I. Block, H. M. Rawel, T. Klamroth, C. Günter, J. Kim, F. Loepthien, S. K. Gahlaut, I. Bald, A. Taubert, *ACS Omega*, 2025, **10**, 4614–4623.
- [13] D. Ghosh Dastidar, S. Saha, M. Chowdhury, Porous microspheres: *Int. J. Pharm.* 2018, **548**, 34–48.
- [14] S. Pöttgen, M. Mazurek-Budzyńska and C. Wischke, *International Journal of Pharmaceutics* 2025, **672**, 125340
- [15] L. Wu, S. Bai and Y. Sun, *Biotechnology Progress*, 2008, **19**, 1300–1306.
- [16] K. J. Stine, *Adv. Carbohydr. Chem. Biochem.*, 2017, **74**, 61–136.
- [17] P. Bayat and P. Rezai, *Soft Matter*. 2018, **14**, 5356.
- [18] J. Oakey, J. Allely, and D. W. M. Marr, *Biotechnol. Prog.* 2002, **18**, 6, 1439.
- [19] M. Yamada, M. Nakashima and M. Seki, *Anal. Chem.* 2004, **76**, 18, 5465.
- [20] J. F. Ashley, C. N. Bowman, and R. H. Davis, *AIChE J.* 2013, **59**, 9, 3444.
- [21] G. Brans, A. Van Dinther, B. Odum, C. G. P. H. Schroën and R. M. Boom, *J. Memb. Sci.* 2007, **290**, 1-2, 230.
- [22] M. Iranmanesh and J. Hulliger, *Chem. Soc. Rev.* 2017, **46**, 5925.
- [23] A. Dalili, E. Samiei, and M. Hoorfar, *Analyst*. 2019, **144**, 87.
- [24] C. Sophonsiri, and E. Morgenroth, *Chemosphere*. 2004, **55**, 5, 691.



- [25] A. Chakra, C. Puijk, G. T. Vladisavljević, C. Cottin-Bizonne, C. Pirat, G. Bolognesi, *Journal of Colloid and Interface Science* 2025, **693**, 137577.
- [26] J. Zheng, J. Chen, Y. Jin, Y. Wen, Y. Mu, C. Wu, Y. Wang, P. Tong, Z. Li, X. Hou, and J. Tang, *Nature* 2023, **617**, 499–506.
- [27] M. Bekir, M. Sperling, D. Vasquez-Muñoz, C. Braksch, A. Böker, N. Lomadze, M. N. Popescu, S. Santer, *Adv. Mater.* 2023, **35**, 2300358.
- [28] D. Vasquez Muñoz, F. Rohne, I. Meier, A. Sharma, N. Lomadze, S. Santer, M. Bekir, *Small* 2024, **20**, 202403546.
- [29] V. Muraveva; M. Bekir; N. Lomadze; R. Großmann, C. Beta, S. Santer, Interplay of diffusio- and thermo-osmotic flows generated by single light stimulus, *Appl. Phys. Lett.* **2022**, *120*, 231905.
- [30] A. Sharma, F. Rohne, D. Vasquez-Muñoz, S.-H. Jung, N. Lomadze, A. Pich, S. Santer, and M. Bekir, *Small Methods* 2024, **8**, 202400226.
- [31] D. Vasquez Munoz, F. Rohne, I. Meier, C. Braksch, N. Lomadze, A. Heraji Esfahani, A. Nitschke, A. Taubert, S. Santer, M. Hartlieb and M. Bekir, *Small Science* 2024, **4**, 2400146.
- [32] D. Vasquez-Muñoz, M. Nicola Popescu, A. Sharma, F. Rohne, I. Meier, P. Ortner, S. Loebner, J. R. Benson, N. Lomadze, S. Eickelmann, S. Santer, M. Bekir, *Small* 2025, **21**, 2500012.
- [33] P. Arya, J. Jelken, N. Lomadze, S. Santer, and M. Bekir, *J. Chem. Phys.* **2020**, *152*, 024904.
- [34] A. Sharma, M. Bekir, N. Lomadze and S. Santer, *Molecules*, 2021, **26**, 19.
- [35] M. Bekir, A. Sharma, M. Umlandt, N. Lomadze and S. Santer, *Adv. Mater. Interf.* 2022, **9**, 2102395.
- [36] F. Rohne, D. Vasquez-Muñoz, S. Santer, M. Bekir, *J. Chromatogr. A.*, **2025**, *1762*, 466368.
- [37] J. Happel, H. Brenner, *Low Reynolds Number Hydrodynamics*, Prentice-Hall, Englewood Cliffs, NJ, **1965**.
- [38] H. Brenner, The slow motion of a sphere through a viscous fluid towards a plane surface, *Chem. Eng. Sci.*, 1961, **16**, 242–251.
- [39] F. Rohne, D. Vasquez Muñoz, I. Meier, N. Lomadze, S. Santer and M. Bekir, *Lab Chip*, 2025, **25**, 4106–4118.
- [40] E. Titov, A. Sharma, N. Lomadze, P. Saalfrank, S. Santer, and M. Bekir, *ChemPhotoChem*, 2021, **5**, 926.
- [41] P.S. Williams, M.H. Moon, Y. Xu, and J.C. Giddings, *Chem. Eng. Sci.*, 1996, **51**, 4477–4488.
- [42] P.S. Williams, T. Koch, and J.C. Giddings, *Chem. Eng. Commun.*, 1991, **111**, 121–147.
- [43] P.S. Williams, L. Seungho, and J.C. Giddings, *Chem. Eng. Commun.*, 1994, **130**, 143–166.
- [44] I. S. Woo, E. C. Jung, S. Lee, *Talanta* 2015, **132**, 945–953.



- [45] A. K. Mathur, C. Agarwal, B. S. Pangtey, A. Singh, B. N. Guptam, *International Journal of Cosmetic Science* 1988, **10**, 213–218.
- [46] J. K. Salem, I. M. El-Nahhal, S. F. Salama, *Chemical Physics Letters* 2019, **730**, 445–450.
- [47] M. Umlandt, D. Feldmann, E. Schneck, S. Santer, M. Bekir, Adsorption of Photoresponsive Surfactants at Solid–Liquid Interface, *Langmuir* **2020**, *36*, 14009.
- [48] F. Rohne, D. Vasquez Muñoz, I. Meier, A. Nitschke, F. Schmitt, N. Lomadze, M. Reifarth, A. Taubert, S. Santer, M. Bekir, Particle-Based Detection of Surface Chemistry via Optical Microscopy—Integrating Microfluidics, Light-Induced Activity of Colloids and Data Science, *Small Methods*, e02329, <https://doi.org/10.1002/smt.202502329>.
- [49] M. Montagna and O. Guskova, “Photosensitive Cationic Azobenzene Surfactants: Thermodynamics of Hydration and the Complex Formation With Poly(methacrylic acid),” *Langmuir* **2018**, *34*, 311–321.
- [50] M. Umlandt, P. Ortner, N. Lomadze, M. Bekir, S. Santer, Y.D. Gordievskaya, *Langmuir* **2025**, *41*, 29567–29577.
- [51] S. Santer, *Journal of Physics D: Applied Physics* **2017**, *51*, 013002.
- [52] M. Bekir, S. Loebner, A. Kobyshev, N. Lomadze, S. Santer, Photosensitive Spherical Polymer Brushes: Light Triggered Process of Particle Repulsion, *Processes* **2023**, *11*, 773.
- [53] M. Bekir, J. Gurke, M. Reifarth, *ChemSystemsChem* **2024**, 202400026.
- [54] M. Schnurbus, R. A. Campbell, J. Droste, C. Honnigfort, D. Glikman, P. Gutfreund, M. R. Hansen, B. Braunschweig, *J. Phys. Chem. B* **2020**, *124*, 6913.
- [55] C. Honnigfort, L. Topp, N. García Rey, A. Heuer, B. Braunschweig, *J. Am. Chem. Soc.* **2022**, *144*, 4026.
- [56] M. Reifarth, M. Bekir, A. M. Bapolisi, E. Titov, F. Nußhardt, J. Nowaczyk, D. Grigoriev, A. Sharma, P. Saalfrank, S. Santer, M. Hartlieb, A. Böker, *Angew. Chem. Int. Ed.* **2022**, *61*, e202114687.
- [57] R. Klajn, *Chem. Soc. Rev.* **2014**, *43*, 148.
- [58] D. H. Waldeck, Photoisomerization Dynamics of Stilbenes, *Chem. Rev.* **1991**, *91*, 415–436.
- [59] L. W. Giles, C. F. J. Faul, R. F. Tabor, *Mater. Adv.* **2021**, *2*, 4152.
- [60] M. J. Boussinesq, *J. Math. Pures Appl.* **1868**, *13*, 377–424.





View Article Online
DOI: 10.1039/D5LF00341E

Institute for Physics and Astronomy

Dr. Marek Bekir
Smart Soft Matter
University of Potsdam
Karl-Liebknecht-Straße 24-25
Building 28
14476 Potsdam-Golm
Phone +49-331-977-5599
marek.bekir@uni-potsdam.de

4th Nov. 2025

Data Availability Statement

The data supporting this article have been included as part of the Supplementary Information.

Primary data (uploaded Video files) supporting this article have been included as part of the Supplementary Information uploaded on publisher website.

A handwritten signature in black ink that reads 'M. Bekir'.

Dr. Marek Bekir

